

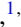




**Frequency-selective spin-wave propagation in magnonic waveguide with a local laser-heated region**V. A. Gubanov <sup>1,\*</sup>, V. V. Kruglyak <sup>2</sup>, S. E. Sheshukova,<sup>1</sup> V. D. Bessonov,<sup>3</sup> S. A. Nikitov <sup>4</sup>, and A. V. Sadovnikov <sup>1</sup><sup>1</sup>*Magnetic Metamaterials, Saratov State University, 410012 Saratov, Russia*<sup>2</sup>*Department of Physics and Astronomy, University of Exeter, Exeter EX4 4QL, United Kingdom*<sup>3</sup>*Institute of Physics of Metals, 620108 Ekaterinburg, Russia*<sup>4</sup>*Kotel'nikov Institute of Radioengineering and Electronics, 125009 Moscow, Russia* (Received 6 April 2022; revised 25 September 2022; accepted 11 October 2022; published 31 January 2023)

We report on the spin-wave propagation along a magnonic waveguide with a local area of decreased magnetization, which is induced by heating produced with a focused laser spot. A phase-sensitive Brillouin light scattering technique is used to image how the spin wave propagates along the waveguide with a local heat landscape. Frequency-selective signal propagation along the waveguide is demonstrated. Micromagnetic simulations reveal intermodal interference variation in the region after the heated area. The proposed way to reconfigure the magnetization landscape can be used in magnonic devices with frequency-selective spin-wave transport.

DOI: [10.1103/PhysRevB.107.024427](https://doi.org/10.1103/PhysRevB.107.024427)**I. INTRODUCTION**

Spin-wave (SW) transport in magnetic microstructures has recently attracted significant attention due to the possibility of using magnonic logic and waveguide structures in energy-efficient devices [1–9]. On the path to overcome the limitations of semiconductor technologies (heat release, dimensional effects, multilayer three-dimensional architectures) [10,11], the use of magnons—quanta of SWs—has enabled generating, transmitting, and processing an information signal in one module. Work is also ongoing to integrate SW logic devices with semiconductor technologies. The first step toward the integration is the process of fabrication of ferromagnetic films on semiconductor substrates [12,13]. Currently, the most promising area of magnonics is the research into SW transport in multidimensional magnonic networks (MNs). MNs are assembled from basic functional blocks with frequency and/or spatial selection of signal propagation [14,15]. Yttrium iron garnet (YIG) [16] is an applicable magnetic material for magnonic waveguides because it offers ultralow magnetic damping and a long SW decay length [17,18].

In MNs the properties of SWs are determined by the dipole and exchange interactions and can be changed significantly by the variation of the parameters of the medium, for example, by a variation in the direction and absolute value of the equilibrium magnetization caused by elastic deformations [13,19], a modification of ferrite film substrate properties by laser radiation [12], or by local laser heating of the ferrite films themselves [20,21]. The concept of surface spin-wave modulation in a garnet film by optical pulses was demonstrated by Fetisov and colleagues [22,23], who showed that fast heating and slow cooling lead to a significant variation of the SW transmission and SW pulse shape. Heating of the YIG

surface distributed along the SW path leads to the scattering of SWs on a nonuniform landscape of magnetization in the form of periodic one-dimensional grating [20], a rectangle or triangle [24], or a circle [25,26]. The local laser illumination of a magnetic film leads to SW channeling along the heating area [26].

Easy-to-fabricate ferromagnetic stripes [27] are the prime candidate for connecting the functional blocks of magnonic units together. In the Damon-Eshbach (DE) configuration [28], SWs propagate along a waveguide that is in plane magnetized normal to the propagating direction. Due to the lateral confinement and quantization in the waveguide's width direction, the SW dispersion contains multiple branches that are hereinafter called width modes. This makes selective SW excitation difficult since the input signal starts to propagate as the sum of the width modes along the waveguide [28,29]. Each mode has its dispersion and magnetization profile. The excitation of SW modes can be controlled, e.g., using tapered waveguides [30,31]. Alternatively, L- and T-shaped magnonic waveguides can be considered [32,33]. In this case the transmission frequency band is narrowed as a result of the intersection of the magnetostatic surface SWs (MSSWs) and the band of backward volume magnetostatic SWs [8,32].

The idea of dipolar SW band intersection was realized using a rectangular or triangular pattern of local heating inside the magnonic waveguide [24]. In the work of Birt *et al.* [34] a circular submicrometer-size defect was fabricated in the center of the magnonic NiFe waveguide. When the SW with an antisymmetric transversal profile propagated through the area with the defect, the channeling regime was observed. Changes in the properties of SW propagation are shown in Refs. [35,36], where a metallic conductor is placed on the YIG film, to which an electric current with a different polarity is applied. When the electric current is applied, the magnetic field changes locally, and the dispersion of the SW changes in that region and leads to the transmission reduction of SWs.

\*vladmeen@gmail.com

For macro- and microscopic YIG magnonic waveguides local heating leads to the transformation of the propagating signal in the form of multimode superposition. The aspect ratio of the magnonic waveguide (width/thickness ratio) defines the uniformity of the internal magnetization profile in the case of DE geometry. The combination of the demagnetization effect and local heating could be used to create a tunable SW interconnection element. Using micromagnetic simulation, we demonstrate the influence of the nonuniform magnetization area inside the waveguide on the SW propagation and width mode interference. We observe how local laser heating transforms SW propagation in the ferromagnetic waveguide for different power values and different diameters of the laser spot. The proposed method of controllable interference of the SW transverse modes can be used in the paradigm of a reconfigurable interconnection element for magnonic devices. Reconfigurability can be interpreted as the variation of the transmission and phase of the SW signal due to the variation of laser light intensity and the diameter of the laser spot focused on the magnonic waveguide.

## II. EXPERIMENTAL LAYOUT AND METHODS

In this work we study the propagation of SWs with a phase resolution in a YIG structure which was fabricated by the space-resolved laser ablation technique. The structure shown in Fig. 1(a) is formed by a YIG [111] film with a thickness of  $s_{\text{YIG}} = 10 \mu\text{m}$  and saturation magnetization  $M_0 = 140 \text{ kA/m}$ . The YIG film was grown on a gadolinium gallium garnet (GGG [111]) substrate with thickness  $s_{\text{GGG}} = 500 \mu\text{m}$ .

The probing of the dynamic magnetization of SWs is performed using the Brillouin light scattering (BLS) spectroscopy technique. This method allows us to detect the precession of magnetization under the excitation of the system with a microwave signal. With the classical BLS system we detected the SW intensity  $I_{\text{BLS}} \sim m_z^2$  [27,37]. By adding an optical phase modulator to the BLS system, the phase of propagating SWs can be measured [38,39].

Figure 1(b) shows the transmission of the light through a phase electro-optical modulator (Newport 4851-02) which was measured by a Sandercock tandem Fabry-Pérot interferometer. Four well-defined peaks are observed in the frequency range from 6.2 to 8.0 GHz. The frequency region with the central frequency  $f_m = 7.35 \text{ GHz}$  is highlighted by the green shaded region in Fig. 1(b). By varying the magnitude of the external magnetic field one can satisfy the condition that the frequency band of the MSSW lie in the region of the operation of the phase modulator at frequency  $f_m$ . The FWHM of this peak was 150 MHz. At the same time, due to significant losses of the SW signal the operation of the phase-resolved scheme is appropriate for the wider frequency band.

Coherent SWs inside the magnonic waveguide can be excited, e.g., by applying a microwave current through a microstrip line or microwave antenna on top of the waveguide or by pure spin current injection [40]. In our scheme the SW excitation was carried out with a  $30 \mu\text{m}$  wide and  $2 \mu\text{m}$  thick gold antenna in the form of  $50 \Omega$  matched microstrip line. The microstrip antenna was located in the input section of the magnonic waveguide [see Fig. 1(a)]. The magnonic waveguide had a width  $w = 2 \text{ mm}$  and a length  $l = 3 \text{ mm}$ . It was

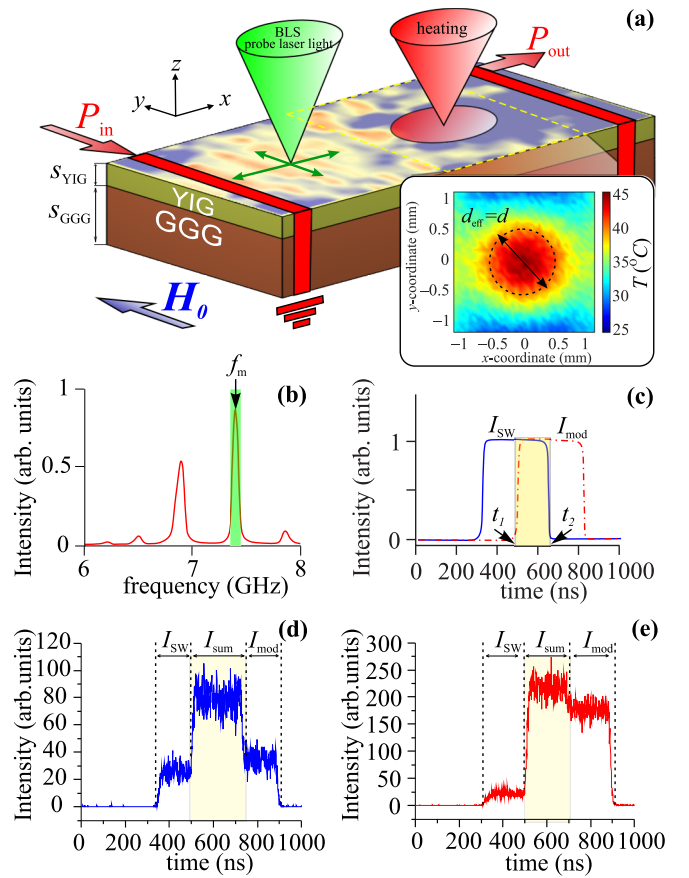


FIG. 1. (a) Sketch of the experimental layout and area of laser illumination. The inset shows heat distribution, obtained by an IR camera in a  $2.3 \times 2.3 \text{ mm}^2$  region of the YIG film. (b) Amplitude-frequency characteristics of the phase modulator and operating frequency bandwidth for experiment, marked in green. (c) Sketch of crossing durations of SW and modulator pulses. The duration of pulses at (d)  $I_{\text{SW}} \sim I_{\text{mod}}$  and (e)  $I_{\text{SW}} < I_{\text{mod}}$ .

placed in the external magnetic field  $H_0 = 1830 \text{ Oe}$  induced by the GMW 3472-70 electromagnet and directed along the  $y$  axis to excite the MSSW [29,41] in the input region of the YIG microwaveguide.

The values of complex  $S$  coefficients were measured using a vector network analyzer (VNA; Agilent E8362C). The amplitude-frequency characteristic was extracted as the frequency dependence of the absolute value of the  $S_{21}$  coefficient in the case when the ports of the VNA were connected to the input  $P_{\text{in}}$  and output  $P_{\text{out}}$  microwave transducers shown in Fig. 1(a). In all experiments the input microwave power was  $-10 \text{ dBm}$  in order to satisfy the condition of linear excitation and propagation of the SW signal [17].

To understand the principle of phase sensitivity it is important to note that the inelastically scattered light, which is detected by the BLS measurements, is determined by both the amplitude and phase of the scattering SW. However, phase information is lost when a photon is received by a photodetector. To obtain the phase information, we use the interference between the inelastically scattered light created as the probing laser beam propagates through the sample and the reference scattered light created by magneto-optical modulation.

To collect data light with a wavelength of 532 nm and a power of 1 mW generated by a single-frequency laser [Excelsior (Spectra Physics) EXLSR-532-200-CDRH] was focused to 25  $\mu\text{m}$  diameter spot on the surface of the YIG structure.

Figure 1(c) shows a schematic sketch of envelopes of two pulses. The pulse denoted by the blue solid line corresponds to the signal which was used to excite the SWs with the microstrip antenna. The pulse indicated by the red dash-dotted curve corresponds to the pulse which was fed to the optical modulator. It should also be noted that to detect the SW phase the frequency ranges of the SW and the optical modulator must overlap. We denote the peak values for the first pulse and second pulse as  $I_{\text{SW}}$  and  $I_{\text{mod}}$ , respectively. The time shift between these two pulses is  $t_2 - t_1 = 190$  ns.

Figures 1(d) and 1(e) demonstrate the experimentally observed intensity of the BLS signal for the case when  $I_{\text{SW}}$  has the same value as  $I_{\text{mod}}$  and  $I_{\text{SW}} < I_{\text{mod}}$ , respectively. The second case occurs due to attenuation of a SW as it propagates along the magnonic waveguide.  $I_{\text{mod}}$  was adjusted to be of the order of  $I_{\text{SW}}$  using a microwave attenuator. Thus, to observe the SW phase the levels of  $I_{\text{SW}}$  and  $I_{\text{mod}}$  should be the same value. During the time window from  $t_1 = 500$  ns to  $t_2 = 690$  ns these two pulses overlap, giving a peak value of the envelope equal to  $I_{\text{sum}}$ , which is denoted by the yellow shaded area in Figs. 1(d) and 1(e). Using this method, the phase of SWs  $I_{\text{phase}}$  was extracted as

$$I_{\text{phase}} = \cos \varphi = \frac{I_{\text{sum}} - I_{\text{mod}} - I_{\text{SW}}}{2\sqrt{I_{\text{mod}}I_{\text{SW}}}}. \quad (1)$$

By performing the point-by-point accumulation of the signal in the whole area of the YIG waveguide, the BLS maps containing the phase and intensity of spin-wave signal are saved. To explain the obtained BLS maps with the phase and intensity of the spin-wave signal inside the magnonic waveguide, we use a micromagnetic simulation of the SW excitation and propagation which was based on a numerical solution of the Landau-Lifshitz-Gilbert equation [42,43]:

$$\frac{\partial \mathbf{M}}{\partial t} = \gamma [\mathbf{H}_{\text{eff}} \times \mathbf{M}] + \frac{\alpha}{M_S(x, y)} \left[ \mathbf{M} \times \frac{\partial \mathbf{M}}{\partial t} \right], \quad (2)$$

where  $\mathbf{M}$  is the magnetization vector,  $\alpha = 10^{-5}$  is the YIG film damping parameter,  $\mathbf{H}_{\text{eff}} = \mathbf{H}_0 + \mathbf{H}_{\text{demag}} + \mathbf{H}_{\text{ex}} + \mathbf{H}_a$  is the effective magnetic field,  $\mathbf{H}_0$  is the external magnetic field,  $\mathbf{H}_{\text{demag}}$  is the demagnetization field,  $\mathbf{H}_{\text{ex}}$  is the exchange field,  $\mathbf{H}_a$  is the anisotropy field, and  $\gamma = 2.8$  MHz/Oe is the gyromagnetic ratio. The open-source GPU accelerated MUMAX<sup>3</sup> [44] software was used. To consider the influence of the local laser heating a circular region with reduced magnetization  $M_S$  was introduced in the simulation. We use the assumption of a linear dependence of the decrease in saturation magnetization with increasing  $T$  since the range of the temperature variation was exceeded by the value of  $T_{\text{RT}} + 15$  K, which is much lower than the Curie temperature  $T_C = 559$  K for YIG. Here  $T_{\text{RT}} = 298$  K is the room temperature. Thus, the variation in temperature leads to the variation in the saturation magnetization in accordance with the linear dependence of magnetization on the temperature [45]:

$$M_S(x, y) \approx M_0 - \beta [T(x, y) - T_{\text{RT}}], \quad (3)$$

where  $\beta = 313$  A/km and  $M_0 = 140$  kA/m is the saturation magnetization at room temperature  $T_{\text{RT}}$ . In the experimental setup, a, 830 nm laser light source was attached to the moving sample holder with the YIG waveguide and was focused in the area located at a distance of 2.2 mm from the input microwave transducer. We use an IR camera to monitor the heating of YIG and the diameter of the laser spot. The maximum value of the temperature increase was 15 K at 500 mW of laser power. We illustrate the heating profile in the inset in Fig. 1(a). The diameter of the laser spot  $d$  is chosen to be the effective diameter of the laser spot  $d_{\text{eff}}$ , obtained from the half height of the laser heating value. Hereafter,  $d = d_{\text{eff}}$  will be assumed in the text.

### III. RESULTS AND DISCUSSION

Figure 2 shows two-dimensional distribution maps for  $I_{\text{phase}}$  and  $I_{\text{SW}}$  obtained from the BLS experiment and the distribution of the  $m_z$  component and map of  $I = m_z^2$  obtained from the micromagnetic simulations. All data are acquired at the frequency  $f = 7.35$  GHz. The left column of Fig. 2 corresponds to the case without local heating, while the right column corresponds to the case of the laser-induced thermal landscape inside the YIG waveguide.

It should be noted that  $I_{\text{phase}}$  is detected by modulating the scanning laser using an optical modulator. It is not correct to directly compare it with the value of  $m_z$ . However, these parameters vary in magnitudes from  $-1$  to  $1$  and show the same nature of the SW propagation in the YIG waveguide. Figures 2(a) and 2(b) show the SW phase distribution in the case without local laser heating, in which there are no reflections. Figures 2(e) and 2(f) show that the SW embraces the heated region with the occurrence of reflections in the YIG waveguide, affecting the wavelength change. Wavelength estimates obtained from both the DE dispersion and the micromagnetic simulations agree with the experimental data.

A micromagnetic simulation was carried out for the case of the experimental heating profile, presented in the inset of Fig. 1. We find that in the case of the nonuniform temperature distribution created in the experiment there is a change in the distribution of the  $m_z$  component in the heated region [Fig. 2(i)], but in the output antenna region (2.5 mm along the  $x$  coordinate) the picture is similar to that in Fig. 2(f). Therefore, in what follows we will consider the case of the uniform heating distribution within the yellow circular region.

Figure 2(c) shows the superposition of the first and third width modes due to wave excitation by the microstrip antenna [28]. To be consistent with the experimental data in the micromagnetic simulation, the profile of the excited SW at the microstrip antenna was introduced by the superposition of the first and third width modes through the sum of two cosines for one and three half wavelengths along the waveguide width [see Fig. 2(d)]. Also, the amplitudes of the excited signal were chosen so that the first mode of the SW has a larger amplitude than the third mode, in agreement with the rule presented in Ref. [29]. The partial reflection of the SW and process of circumflexing the heated region are easily distinguished in the BLS data and micromagnetic simulation for the case when the laser heating was performed at a distance of 2.2 mm from the transducer. Here we emphasize that the

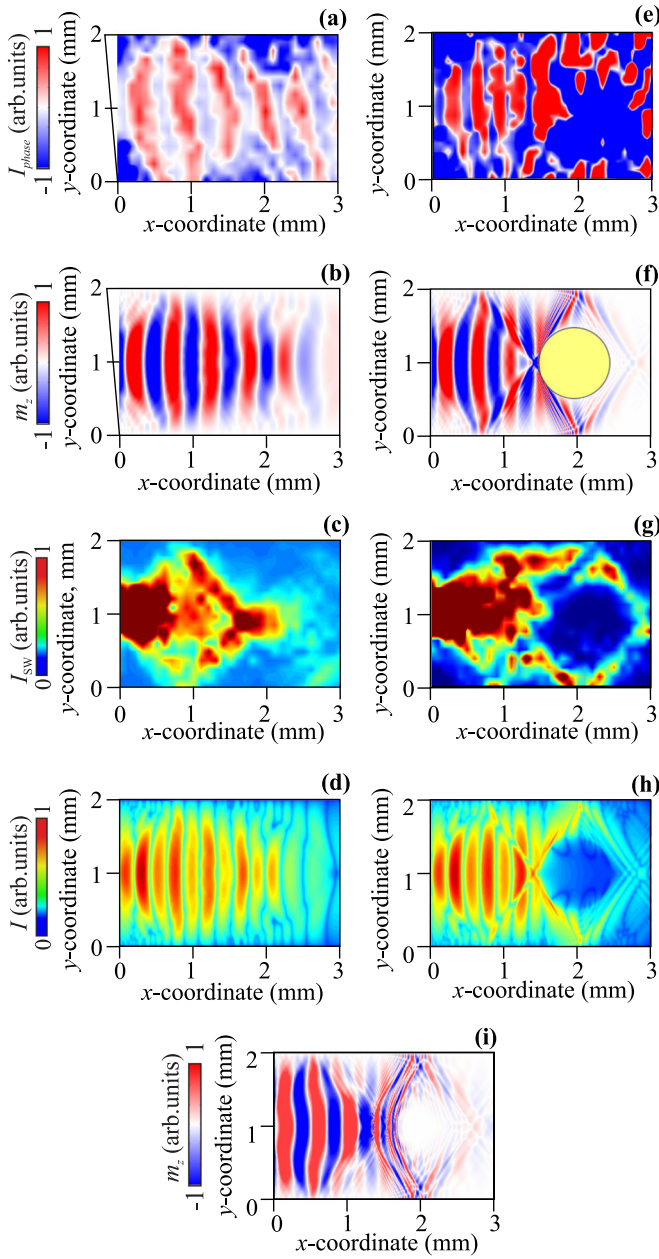


FIG. 2. Two-dimensional distribution maps for (a) and (e)  $I_{\text{phase}}$  and (c) and (g)  $I_{\text{SW}}$ , obtained from the BLS experiment, and (b) and (f) distribution of the  $m_z$  component and (d) and (h) map of  $I = m_x^2 + m_z^2$  obtained from the micromagnetic simulations. All data are acquired at the frequency  $f = 7.35$  GHz. Left: case without local heating; right: case with the laser-induced thermal landscape inside the YIG waveguide, marked by the yellow circular region in (f) as an example. (i) The distribution of the  $m_z$  component for the magnetization profile corresponding to the experimental heat distribution.

transformation of the SW propagation regime is observed. Local laser heating produces conditions for transformation of the mode composition inside the waveguide: the first width mode is interfered with the third width mode. And the third width mode propagates around the area with local laser heating. Figures 2(e) and 2(f) demonstrate how the transformation

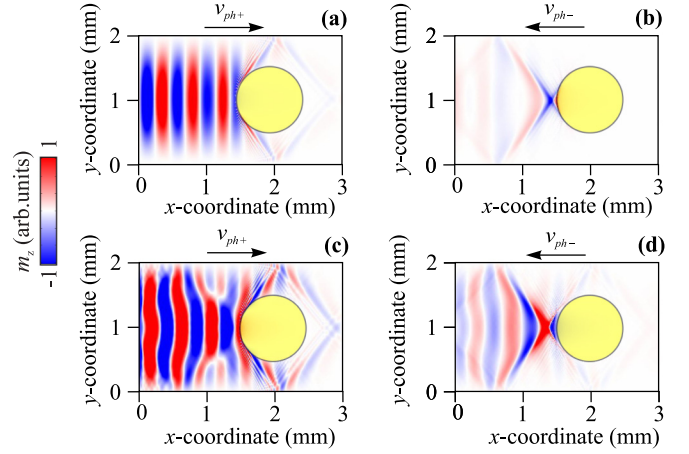


FIG. 3. The distribution of the  $m_z$  component of (a) and (b) the SW for the first width mode and (c) and (d) superposition first and third width mode SW excitation in the case of the laser-induced thermal landscape inside the YIG waveguide (yellow circular region). Left: SW with  $k_+$  wave numbers; right: SW with  $k_-$  wave numbers. The simulation was performed at the excitation frequency  $f = 7.35$  GHz.

of the magnetization distribution produced by heating results in the SW signal rejection.

To show the process of SW reflection from the heated area the following steps were performed during the numerical simulation [25]. First, the distribution of the  $m_z$  component over the whole structure at the excitation frequency  $f = 7.35$  GHz was saved with time step  $\Delta t = \frac{\pi}{2f} = \frac{T}{4}$  to form the time-coordinate data array  $\hat{M} = m_z(x, y, p\Delta t)$ , where  $p = 0, 1, 2, \dots$ . The two-dimensional Fourier transform of  $\hat{M}$  was performed to obtain  $F(k_x, k_y, \omega)$ , where  $\omega = 2\pi f$  is the circular frequency. Two independent data arrays,  $F_+$  and  $F_-$ , were constructed by zeroing the  $k_-$  and  $k_+$  regions of  $F(k_x, k_y, \omega)$ , respectively; thus,

$$F_- = \begin{cases} F(k_x, k_y, \omega), & \text{if } k_x < 0, \\ 0, & \text{if } k_x > 0, \end{cases} \quad (4)$$

$$F_+ = \begin{cases} 0, & \text{if } k_x < 0, \\ F(k_x, k_y, \omega), & \text{if } k_x > 0. \end{cases} \quad (5)$$

Next, we performed the inverse two-dimensional Fourier transform of  $F_+$  and  $F_-$  to obtain the  $\hat{M}_+$  and  $\hat{M}_-$  arrays, respectively. By plotting  $\hat{M}_{+,-}(x, y, t = 75 \text{ ns})$  the waves propagating in the positive and negative directions of the  $x$  axis were extracted (see Fig. 3). Figure 3 shows the results of the micromagnetic simulation and the above-described Fourier transform for the excitation first width mode [Figs. 3(a) and 3(b)] and the superposition of the first and third width modes [Figs. 3(c) and 3(d)]. Figures 3(a) and 3(c) correspond to the positive  $x$  projection of the phase velocity  $v_{\text{ph}+}$ , while data in Figs. 3(b) and 3(d) are related to the negative  $x$  projection of the phase velocity  $v_{\text{ph}-}$ . As can be seen, in the case of the first and third width mode excitation, the reflection is more pronounced than for the single-mode regime. Also according to the obtained data it is possible to estimate the reflection coefficient of the SW from the heated area. The distribution map of the  $m_z$  component in the case

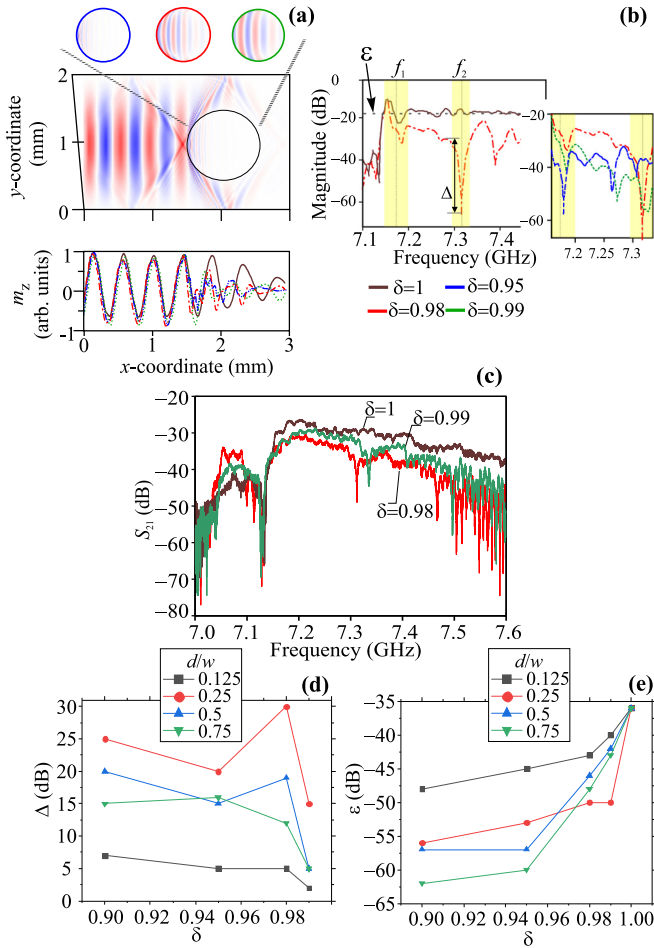


FIG. 4. Results of micromagnetic simulations. (a) Distribution of the  $m_z$  component and its integral along the  $y$  axis with the diameter of the heated area equal to  $1000 \mu\text{m}$ . The inset presents SW profiles in the heated region for the following cases of decreased magnetization:  $\delta = 0.95$  (blue circle),  $\delta = 0.98$  (red circle), and  $\delta = 0.99$  (green circle). (b) Transmission characteristics, observed by the micromagnetic simulation in the output antenna  $P_{\text{out}}$  for different values of heating. The inset shows transmission spectra for different values of  $\delta$ :  $\delta = 0.95$ ,  $\delta = 0.98$ , and  $\delta = 0.99$ . (c) Transfer characteristics obtained by the microwave experiment for different strengths of heating. (d) Value of transmission dips  $\Delta$  and (e) average level of transmission  $\epsilon$  in cases with different laser heating areas from  $d/w = 0.125$  to  $0.75$  as a function of the magnetization due to the local laser heating.

of the backward propagating wave reveals that the reflection (scattering) occurs at the edge of the heated region, at a distance of  $2.2 \text{ mm}$ .

By performing the micromagnetic simulation we revealed how the diameter of the laser light spot and the strength of heating transform the SW propagation inside the stripe waveguide. Here we introduce a term to describe the change in saturation magnetization:  $\delta = M_S/M_0$ , where  $M_S$  is the magnetization saturation in the heated area and  $M_0$  is the magnetization saturation in the rest of the YIG waveguide, which corresponds to magnetization at room temperature in accordance with our model. Figure 4(a) demonstrates the distribution of the  $m_z$  component, revealed

by micromagnetic simulations with the diameter of the heated area equal to  $d = 1000 \mu\text{m}$  and varying values of  $\delta$ . Inside the heated region the wavelength is reduced, as expected for the lower magnetization in the case of MSSWs. At the same time excitation of high-order width modes in the region of reduced magnetization is observed. The bottom part of Fig. 4(a) shows the value of  $m_z$  integrated along the  $y$  axis. In the heated region there is a decrease in the integrated value of  $m_z$ , and the wavelength changes according to the modification of the dispersion relation by the reduced magnetization.

The dispersion relation for the finite-width YIG waveguide [28] was used to describe the transformation of SW wave numbers for the wave propagating inside and beyond the area of the heated region:

$$e^{2Ms} = \frac{\Omega_H M + \Omega k + F(M - N)}{\Omega_H M - \Omega k + F(M + N)} \times \frac{\Omega_H M - \Omega k + F[M - N \tanh(Ns)]}{\Omega_H M + \Omega k + F[M + N \tanh(Ns)]}, \quad (6)$$

where  $\Omega_H(T) = H/4\pi M_S(T)$ ,  $\Omega(T) = \omega/[4\pi M_S(T)]$ ,  $F = \Omega_H^2 - \Omega^2$ ,  $M = \sqrt{(n\pi/w)^2 + \mu_1 + k_x^2}$ ,  $N = \sqrt{(n\pi/w)^2 + k_x^2}$ ,  $\mu_1 = 1 - \Omega_H/(\Omega^2 - \Omega_H^2)$ ,  $k$  is the wave number,  $k_x$  is the  $x$  component of the wave number, and  $s$  is the thickness of the film.

The estimation of the differences between the longitudinal wave numbers of the first ( $k_1$ ) and third ( $k_3$ ) width modes  $\Delta k_{13} = |k_3 - k_1|$  with the variation of the temperature and  $M_S$  shows that  $\Delta k_{13}$  is about  $15 \text{ cm}^{-1}$  when  $\delta$  varies from 1 to 0.95. This can be used to estimate the mode beating length, which varies with the variation of  $\Delta k_{13}$ . In the case of decreasing the magnetization and the parameter  $\delta$  to the value  $\delta = 0.95$  inside the circular region the SW wavelength decreases, and the SW amplitude also decreases. Thus, the local area with the varying magnetization acts as a resonator inside the magnonic waveguide. In other words, the structure could be considered a connection between two spin-wave waveguides with the resonator placed between them. When the parameter  $\delta \rightarrow 1$  is increased, the coupling parameter between the unheated region of the waveguide and the resonator region increases. This effect of increasing the coupling between the waveguide modes and standing SW modes of the resonator is described in more detail in Ref. [46].

To characterize operating regimes when the heated area is  $d = 500 \mu\text{m}$ , transfer characteristics with different values of laser heating (decreasing magnetization) were obtained. We take the information in output port  $P_{\text{out}}$  as being integrated along the  $y$ -axis  $m_z$  component magnetization and plot the transfer characteristics in Fig. 4(b). As we see, for the transfer characteristics there exist two frequency areas with decreasing spin-wave transmission with central frequencies  $f_1 = 7.18 \text{ GHz}$  and  $f_2 = 7.31 \text{ GHz}$ . It can be seen that the average transmission level  $\epsilon$  of the spin-wave signal decreases as the laser power value is increased. It is also important to note that a dip appears in the amplitude-frequency response when laser radiation is applied. The depth of the dip is denoted as  $\Delta$ . Figure 4(c) shows the results for the experimentally measured transfer characteristics  $S_{21}$  using the microwave spectroscopy technique based on the E8362C PNA VNA. As can be seen, in the frequency range of  $7.3 \text{ GHz}$  there are

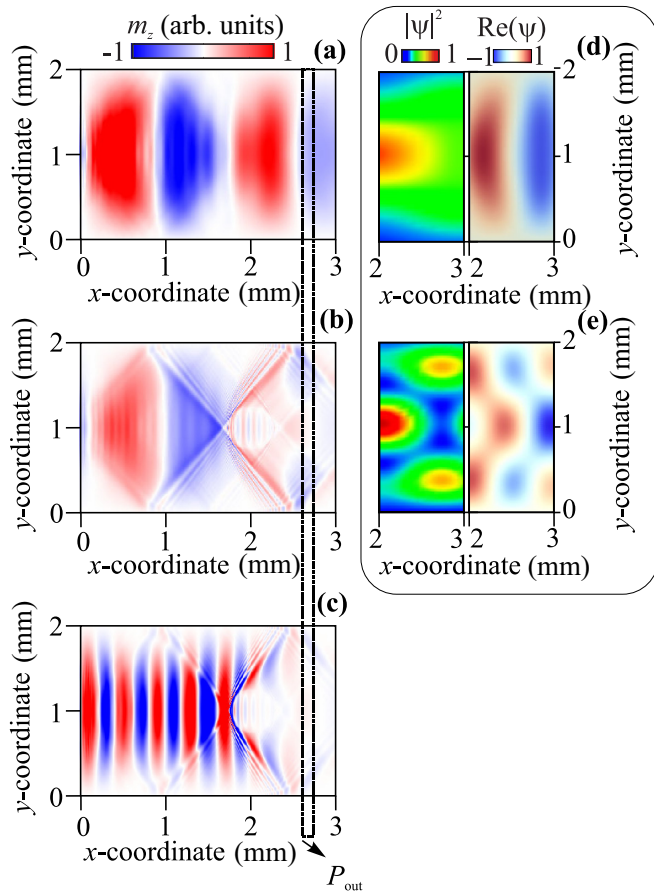


FIG. 5. Distribution of the  $m_z$  component of the magnetization with different decreasing values of magnetization relative to the normal value of  $M_0$  at  $d/w = 0.25$ : (a)  $\delta = 1$  (without heating) for  $f_1 = 7.18$  GHz, (b)  $\delta = 0.99$  for  $f_1 = 7.18$  GHz, and (c)  $\delta = 0.98$  for  $f_2 = 7.31$  GHz. Calculated maps of  $|\psi|^2$  and  $\text{Re}(\psi)$  for (d) the first width mode and (e) superposition of the first and the third width modes.

dips in the transmission of the information signal, as in the micromagnetic simulation.

Next, it is important to observe how the average transmission level  $\varepsilon$  and the depth of the dip  $\Delta$  change when the parameter  $\delta$  is changed.

Figures 4(d) and 4(e) demonstrate the  $\Delta$  and  $\varepsilon$  dependences of the value of the parameter  $\delta$  on the laser-heated area from  $d/w = 0.125$  to  $0.75$ . As we specified  $d_{\text{eff}}$  as the peak width at half maximum in the temperature profile of the heating area, we consider  $d$  and the temperature difference to be separate parameters. Generally, the temperature difference and the diameter of the heated zone are not independent.

It should be noted that for  $\delta$  ranging from 1 to 0.98  $\varepsilon$  varies particularly strongly, forming a linear dependence for stronger heating. Thus, the main contribution to the transfer characteristic is made by heating by 10 K relative to room temperature. As we can see, at the value  $d/w = 0.25$  there is a maximum dip in the transfer characteristic at the optimum transfer level.

As we can see in the slice  $P_{\text{out}}$  in Fig. 5(a), the phase distribution of SWs is homogeneous. This regime is suitable

for SW propagation with maximum power at the output antenna. However, in Figs. 5(b) and 5(c) we observe regimes where the character of SW propagation changes: now in the slice output antenna the phase is nonhomogeneous: mixed positive (red) and negative (blue) phases. If we integrate the data, the resulting magnetization will be smaller than that in the case without laser heating, which is the reason for the dips in the transmission characteristics.

To understand the multimode regime, we obtained distribution maps of the amplitude for the superposition of the first and third width modes using the following equation:

$$\psi(x, y) = a_1 e^{ik_{x1}x} + a_3 e^{ik_{x3}x}, \quad (7)$$

where  $a_{1,3}$  are the amplitudes of signals of the first and third width modes.  $\psi$  was obtained without considering local laser heating. The parameters were chosen to describe the mode in Figs. 5(a) and 5(b) in the 2 to 3 mm waveguide region along the  $x$  axis. Figures 5(d) and 5(e) plot the distribution maps  $|\psi|^2$  and  $\text{Re}(\psi)$ . It can be seen that for the first width mode [Figs. 5(a) and 5(d)] in the output antenna the maximum signal is observed. Values of amplitudes  $a_{1,3}$  for the first width mode were chosen according to experiment:  $a_1 = 0.9$  and  $a_3 = 0.1$ . In the case of local heating the multimode regime is observed in the region after the SW passes the heated circle area. To prove this a color-coded map is depicted in Fig. 5(e) for the case with  $a_1 = 0.9$  and  $a_3 = 0.75$ . It can be seen that in the region with the third width mode along the  $y$  coordinate there is a negative value of  $\text{Re}(\psi)$  for the first width mode. This distribution is very different from the case for the first width mode. Based on the transfer characteristics, we can conclude that a small amount of heating (to about 10 K above room temperature in order to reduce the value of  $\delta$  to  $\delta = 0.98$ ) is necessary to create a multimode regime for the SW propagation.

The proposed mechanism of mode filtering is consistent with the concept considered in Ref. [34], where the observed spot splitting was associated with the propagation of the anti-symmetric mode (second-order width mode) through the area with a small antidot placed in the center of the magnonic waveguide. In the proposed concept the reconfigurability is achieved using the variation of the laser beam power and diameter. At the same time the SW tunneling through the barrier in the form of nonuniformity of the magnetic field was observed and described in Refs. [35,36]. We suggest that SW transmission variation using the laser light spot can be described using the theoretical approach which was developed in Ref. [36] for the single-mode regime of SW propagation.

The presented mechanism of spin-wave control is appropriate as an alternative for other methods, such as nonlinearity, straintronics, translation symmetry breaking, magnonic crystals, etc. Local heating of the magnonic waveguide is a versatile method of spin-wave phase and amplitude control. Here we have proposed a proof of concept of such a device. To perform spin-wave propagation control we need a SW source (here we use microwave current), a YIG film as a bus for SWs, a control unit (focused laser light), and an output microwave antenna.

#### IV. CONCLUSION

In conclusion, the effect of laser heating on the propagation of SWs in the YIG waveguide was investigated. It was shown that by changing the value of local laser heating in the region with decreasing magnetization, the phase of SWs decreases. It was also shown that the SW is able to go around the heated region and there are also regimes in which the transmission of the SW deteriorates. This is based on the effect of SW interference. Using the BLS method and adding an optical phase modulator to the optical system, the phase of the SW and the effect of heating were experimentally demonstrated. The experimental data agree with the micromagnetic simulation results. It was shown that by varying the heating strength, the

transfer characteristics can be changed and parameters such as the average transmission level  $\epsilon$  and the  $\Delta$  depth of the dip can be controlled. Based on micromagnetic modeling, it was found that to obtain a nontransmittance mode, the structure should be heated to 10 K above room temperature. The proposed method of controlled interference with transverse modes of SWs can be used to create a configurable coupler for magnon devices.

#### ACKNOWLEDGMENT

This work was supported by the Russian Science Foundation (Project No. 20-79-10191).

- 
- [1] A. B. Ustinov and B. A. Kalinikos, A microwave nonlinear phase shifter, *Appl. Phys. Lett.* **93**, 102504 (2008).
- [2] A. V. Chumak, V. I. Vasyuchka, A. A. Serga, and B. Hillebrands, Magnon spintronics, *Nat. Phys.* **11**, 453 (2015).
- [3] Q. Wang, P. Pirro, R. Verba, A. Slavin, B. Hillebrands, and A. V. Chumak, Reconfigurable nanoscale spin-wave directional coupler, *Sci. Adv.* **4**, e1701517 (2018).
- [4] V. V. Kruglyak, S. O. Demokritov, and D. Grundler, Magnonics, *J. Phys. D* **43**, 264001 (2010).
- [5] A. B. Ustinov, E. L ahderanta, M. Inoue, and B. A. Kalinikos, Nonlinear spin-wave logic gates, *IEEE Magn. Lett.* **10**, 5508204 (2019).
- [6] K. Vogt, F. Fradin, J. Pearson, T. Sebastian, S. Bader, B. Hillebrands, A. Hoffmann, and H. Schultheiss, Realization of a spin-wave multiplexer, *Nat. Commun.* **5**, 3727 (2014).
- [7] A. V. Chumak, A. A. Serga, and B. Hillebrands, Magnon transistor for all-magnon data processing, *Nat. Commun.* **5**, 4700 (2014).
- [8] A. Sadovnikov, E. Beginin, S. Sheshukova, D. Romanenko, Y. P. Sharaevskii, and S. Nikitov, Directional multimode coupler for planar magnonics: Side-coupled magnetic stripes, *Appl. Phys. Lett.* **107**, 202405 (2015).
- [9] A. Barman *et al.*, The 2021 magnonics roadmap, *J. Phys.: Condens. Matter* **33**, 413001 (2021).
- [10] M. Neisser and S. Wurm, ITRS lithography roadmap: 2015 challenges, *Adv. Opt. Technol.* **4**, 235 (2015).
- [11] E. N. Beginin, D. V. Kalyabin, P. A. Popov, A. V. Sadovnikov, A. Y. Sharaevskaya, A. I. Stognij, and S. A. Nikitov, 3D magnonic crystals, in *Three-Dimensional Magnonics*, edited by G. Gubbiotti (Jenny Stanford Publishing, New York, 2019), pp. 67–104.
- [12] A. V. Sadovnikov, E. N. Beginin, S. E. Sheshukova, Y. P. Sharaevskii, A. I. Stognij, N. N. Novitski, V. K. Sakharov, Y. V. Khivintsev, and S. A. Nikitov, Route toward semiconductor magnonics: Light-induced spin-wave nonreciprocity in a YIG/GaAs structure, *Phys. Rev. B* **99**, 054424 (2019).
- [13] A. V. Sadovnikov, A. A. Grachev, A. A. Serdobintsev, S. E. Sheshukova, S. S. Yankin, and S. A. Nikitov, Magnon straintronics to control spin-wave computation: Strain reconfigurable magnonic-crystal directional coupler, *IEEE Magn. Lett.* **10**, 5506405 (2019).
- [14] S. A. Nikitov, A. R. Safin, D. V. Kalyabin, A. V. Sadovnikov, E. N. Beginin, M. V. Logunov, M. A. Morozova, S. A. Odintsov, S. A. Osokin, A. Y. Sharaevskaya, Y. P. Sharaevsky, and A. I. Kirilyuk, Dielectric magnonics: From gigahertz to terahertz, *Phys. Usp.* **63**, 945 (2020).
- [15] Y. V. Khivintsev, V. K. Sakharov, A. V. Kozhevnikov, G. M. Dudko, Y. A. Filimonov, and A. Khitun, Spin waves in YIG based magnonic networks: Design and technological aspects, *J. Magn. Magn. Mater.* **545**, 168754 (2021).
- [16] V. Cherepanov, I. Kolokolov, and V. L'vov, The saga of YIG: Spectra, thermodynamics, interaction and relaxation of magnons in a complex magnet, *Phys. Rep.* **229**, 81 (1993).
- [17] A. G. Gurevich and G. A. Melkov, *Magnetization Oscillations and Waves*, 1st ed. (CRC Press, 1996).
- [18] W. S. Ishak, Magnetostatic wave technology: A review, *Proc. IEEE* **76**, 171 (1988).
- [19] N. S. Gusev, A. V. Sadovnikov, S. A. Nikitov, M. V. Sapozhnikov, and O. G. Udalov, Manipulation of the Dzyaloshinskii–Moriya Interaction in Co/Pt Multilayers with Strain, *Phys. Rev. Lett.* **124**, 157202 (2020).
- [20] M. Vogel, A. V. Chumak, E. H. Waller, T. Langner, V. I. Vasyuchka, B. Hillebrands, and G. von Freymann, Optically reconfigurable magnetic materials, *Nat. Phys.* **11**, 487 (2015).
- [21] P. Borys, O. Kolokoltsev, I. G omez-Arista, I. V. Zavislyak, G. A. Melkov, N. Qureshi, and C. L. Ord o nez-Romero, Thermally controlled confinement of spin wave field in a magnonic YIG waveguide, *J. Magn. Magn. Mater.* **498**, 166154 (2020).
- [22] S. Dunaev and Y. Fetisov, Effect of pulsed optical heating on magnetostatic wave propagation in ferrite film, *IEEE Trans. Magn.* **31**, 3488 (1995).
- [23] Y. K. Fetisov and A. V. Makovkin, Modulation of magnetostatic surface wave in garnet film by optical pulses, *J. Appl. Phys.* **79**, 5721 (1996).
- [24] M. Vogel, R. A mann, P. Pirro, A. V. Chumak, B. Hillebrands, and G. von Freymann, Control of spin-wave propagation using magnetisation gradients, *Sci. Rep.* **8**, 11099 (2018).
- [25] N. J. Whitehead, S. A. R. Horsley, T. G. Philbin, and V. V. Kruglyak, A Luneburg lens for spin waves, *Appl. Phys. Lett.* **113**, 212404 (2018).
- [26] O. Dzyapko, I. Borisenko, V. Demidov, W. Pernice, and S. Demokritov, Reconfigurable heat-induced spin wave lenses, *Appl. Phys. Lett.* **109**, 232407 (2016).
- [27] S. Demokritov, Brillouin light scattering studies of confined spin waves: Linear and nonlinear confinement, *Phys. Rep.* **348**, 441 (2001).

- [28] T. W. O’Keeffe and R. W. Patterson, Magnetostatic surface-wave propagation in finite samples, *J. Appl. Phys.* **49**, 4886 (1978).
- [29] S. N. Bajpai, Excitation of magnetostatic surface waves: Effect of finite sample width, *J. Appl. Phys.* **58**, 910 (1985).
- [30] D. V. Kalyabin, A. V. Sadovnikov, E. N. Beginin, and S. A. Nikitov, Surface spin waves propagation in tapered magnetic stripe, *J. Appl. Phys.* **126**, 173907 (2019).
- [31] V. Demidov, M. Kostylev, K. Rott, J. Münchenberger, G. Reiss, and S. Demokritov, Excitation of short-wavelength spin waves in magnonic waveguides, *Appl. Phys. Lett.* **99**, 082507 (2011).
- [32] T. Brächer, P. Pirro, J. Westermann, T. Sebastian, B. Lägél, B. Van de Wiele, A. Vansteenkiste, and B. Hillebrands, Generation of propagating backward volume spin waves by phase-sensitive mode conversion in two-dimensional microstructures, *Appl. Phys. Lett.* **102**, 132411 (2013).
- [33] A. V. Sadovnikov, C. S. Davies, V. V. Kruglyak, D. V. Romanenko, S. V. Grishin, E. N. Beginin, Y. P. Sharaevskii, and S. A. Nikitov, Spin wave propagation in a uniformly biased curved magnonic waveguide, *Phys. Rev. B* **96**, 060401(R) (2017).
- [34] D. R. Birt, B. O’Gorman, M. Tsoi, X. Li, V. E. Demidov, and S. O. Demokritov, Diffraction of spin waves from a submicrometer-size defect in a microwaveguide, *Appl. Phys. Lett.* **95**, 122510 (2009).
- [35] S. O. Demokritov, A. A. Serga, A. André, V. E. Demidov, M. P. Kostylev, B. Hillebrands, and A. N. Slavin, Tunneling of Dipolar Spin Waves through a Region of Inhomogeneous Magnetic Field, *Phys. Rev. Lett.* **93**, 047201 (2004).
- [36] M. P. Kostylev, A. A. Serga, T. Schneider, T. Neumann, B. Leven, B. Hillebrands, and R. L. Stamps, Resonant and nonresonant scattering of dipole-dominated spin waves from a region of inhomogeneous magnetic field in a ferromagnetic film, *Phys. Rev. B* **76**, 184419 (2007).
- [37] *Modern Techniques for Characterizing Magnetic Materials*, edited by Y. Zhu (Springer, Boston, MA, 2005).
- [38] A. A. Serga, T. Schneider, B. Hillebrands, S. O. Demokritov, and M. P. Kostylev, Phase-sensitive Brillouin light scattering spectroscopy from spin-wave packets, *Appl. Phys. Lett.* **89**, 063506 (2006).
- [39] V. E. Demidov, S. Urazhdin, and S. O. Demokritov, Control of spin-wave phase and wavelength by electric current on the microscopic scale, *Appl. Phys. Lett.* **95**, 262509 (2009).
- [40] V. E. Demidov, S. Urazhdin, R. Liu, B. Divinskiy, A. Telegin, and S. O. Demokritov, Excitation of coherent propagating spin waves by pure spin currents, *Nat. Commun.* **7**, 10446 (2016).
- [41] R. Damon and J. Eshbach, Magnetostatic modes of a ferromagnet slab, *J. Phys. Chem. Solids* **19**, 308 (1961).
- [42] L. Landau and E. Lifshitz, On the theory of the dispersion of magnetic permeability in ferromagnetic bodies, *Perspectives in Theoretical Physics* (Pregamon, 1992), Chap. 3, pp. 51–65.
- [43] T. L. Gilbert, A Lagrangian formulation of the gyromagnetic equation of the magnetization field, *Phys. Rev.* **100**, 1243 (1955).
- [44] A. Vansteenkiste, J. Leliaert, M. Dvornik, M. Helsen, F. Garcia-Sanchez, and B. V. Waeyenberge, The design and verification of MuMax3, *AIP Adv.* **4**, 107133 (2014).
- [45] A. Prabhakar and D. D. Stancil, *Spin Waves: Theory and applications* (Springer, New York, 2009), Vol. 5.
- [46] A. A. Grachev, E. N. Beginin, S. E. Sheshukova, and A. V. Sadovnikov, Tunable Fano resonances in irregular magnonic structure, *IEEE Trans. Magn.* **58**, 1300205 (2021).